

Cite this: *J. Mater. Chem. C*, 2022, **10**, 13946

## A zero-field single-molecule magnet with luminescence thermometry capabilities containing soft donors†

Riccardo Marin,<sup>†</sup> Diogo Alves Gálico,<sup>†</sup> Rezeda Gayfullina,<sup>†</sup> Jani O. Moilanen,<sup>†</sup> Luís D. Carlos,<sup>†</sup> Daniel Jaque<sup>†</sup> and Muralee Murugesu<sup>†</sup>

Simultaneous fine-tune of magnetic and optical properties in lanthanide single-molecule magnets (SMMs) is a daunting task. Even more so when additional functionalities, like luminescence thermometry, are sought after. Herein, we explore the use of a ligand with both soft and hard donor atoms (thiobenzoate, tba<sup>-</sup>) as a strategy to prepare a multifunctional optomagnetic lanthanide complex. The proposed mononuclear Dy<sup>3+</sup> complex acts as a zero-field SMM, whose energy barrier to magnetization reversal was confirmed from the analysis of the photoluminescence spectrum. Moreover, the temperature dependence of the emission spectral profile was harnessed to build a thermometric approach working below 12 K – where the complex behaves as an SMM. In search for general trends informing the preparation of similar multifunctional SMMs, we modelled the electronic properties of a series of complexes where the sulfur atom of tba<sup>-</sup> is replaced for other chalcogens (O, Se, Te). These calculations show that careful choice of ligands with soft donor atoms can boost both magnetic and thermometric performances, paving the way for the rational design of novel multifunctional lanthanide complexes.

Received 21st April 2022,  
Accepted 23rd June 2022

DOI: 10.1039/d2tc01661c

rsc.li/materials-c

## Introduction

In the fast-paced digital era, information is created and exchanged at an unprecedented rate, thus requiring increasingly efficient physical storage units. In addition, electronic devices are undergoing extreme miniaturization and the first case of “quantum supremacy” – *i.e.*, a quantum processor outperforming a classical computer – was recently reported.<sup>1</sup>

In the frame of this digital revolution, single-molecule magnets (SMMs) are prime candidates for becoming building blocks of the next-generation of electronic devices. Lanthanide (Ln<sup>3+</sup>) complexes are the cream of the crop of this family of compounds,<sup>2–4</sup> with working temperatures recently reaching the boiling point of liquid nitrogen, bringing these species one step closer to real-world applications.<sup>5</sup>

To ensure the proper functioning of an SMM, its temperature should be controlled and maintained below a specific threshold. To that end, we reported the first examples of Ln<sup>3+</sup>-SMMs whose photoluminescence (PL) can be harnessed to monitor their thermal state.<sup>6–11</sup> However, the preparation of Ln<sup>3+</sup>-complexes simultaneously performing well as SMMs and luminescent thermometers is no easy task, and it requires judicious choice of the ligand framework, metal, and coordination geometry.<sup>8,12</sup> In this context, ligands containing soft donors like heavy chalcogens (E = S, Se, Te) hold promise. This is because the large radial extension of their valence orbitals affects the ligand field around the metal centre. Ln–E bonds have also lower associated vibrational energies compared to Ln–O bonds. Not only this promotes high barrier to magnetization reversal ( $U_{\text{eff}}$ ),<sup>13,14</sup> but also supports efficient Ln<sup>3+</sup> PL.<sup>15</sup> Yet, these ligands are underexplored compared to N- and O-containing ligands.

Moving from these considerations, we propose the first example of soft-donor-containing SMM acting as luminescent

<sup>a</sup> Nanomaterials for Bioimaging Group (nanoBIG), Departamento de Física de Materiales, Facultad de Ciencias, Universidad Autónoma de Madrid, C/Francisco Tomás y Valiente 7, Madrid, 28049, Spain. E-mail: riccardo.marin@uam.es

<sup>b</sup> Department of Chemistry and Biomolecular Sciences, University of Ottawa, Ottawa, Ontario, K1N 6N5, Canada. E-mail: m.murugesu@uottawa.ca

<sup>c</sup> Department of Chemistry, Nanoscience Centre, University of Jyväskylä, P.O. Box 35, FI-40014, Finland

<sup>d</sup> Phantom-g, CICECO – Aveiro Institute of Materials, Department of Physics, Universidade de Aveiro, 3810-193, Aveiro, Portugal

<sup>e</sup> Nanomaterials for Bioimaging Group (nanoBIG), Instituto Ramón y Cajal de Investigación Sanitaria, Hospital Ramón y Cajal, Ctra. De Colmenar Viejo, Km. 9100, 28034, Madrid, Spain

† Electronic supplementary information (ESI) available: Experimental details, structural and chemical characterization, additional magnetic data, mathematical treatment of luminescence thermometry, computational details and simulation of the thermometric performance. CCDC 2167973. For ESI and crystallographic data in CIF or other electronic format see DOI: <https://doi.org/10.1039/d2tc01661c>

‡ These authors contributed equally to this work.

thermometer in the form of a novel thiobenzoate ( $\text{tba}^-$ )-based  $\text{Dy}^{3+}$  complex:  $[\text{Dy}(\text{tba})_3\text{phen}]\cdot\text{CH}_2\text{Cl}_2$  (**1**; phen = 1,10-phenanthroline). This complex brings together the stable Ln–O interaction along with the property-modulating features imparted by Ln–S bonds. Analysis of the photoluminescence (PL) spectrum allowed interpreting the magnetic relaxation mechanism of this zero-field SMM, while the temperature-dependent spectral variations were harnessed to develop a luminescence thermometric approach. Stimulated by these results, we deepened our exploration of soft-donor-containing ligands for tuning optical and magnetic features in complexes with the use of *ab initio* and density functional theory calculations. Modelling of a series of  $\text{Dy}^{3+}$  complexes generated from **1** replacing  $\text{tba}^-$  for benzoate, selenobenzoate, and tellurobenzoate show trends of optical and magnetic properties that highlight how soft donor atoms can be valuable allies in pursuit of luminescent SMMs with thermometric capabilities.

## Results and discussion

### Structural characterization

$[\text{Dy}(\text{tba})_3\text{phen}]\cdot\text{CH}_2\text{Cl}_2$  (**1**) was synthesized by adding an aqueous solution of  $\text{Dy}(\text{NO}_3)_3\cdot 5\text{H}_2\text{O}$  to a solution of potassium thiobenzoate (Ktba) and phen in water (Ktba : phen = 3 : 1). The precipitated yellow powder was recrystallized from dichloromethane (DCM), yielding transparent pale yellow crystals with needle-like morphology. Details about the experimental procedure are given in the ESI.† Complex **1** crystallizes in the monoclinic  $P2_1/c$  space group, with one DCM crystallization molecule for every complex molecule in the structure (Fig. 1, Fig. S1 and Table S1, ESI†).



**Riccardo Marin**

*Riccardo Marin obtained his PhD in Chemistry jointly from the University Ca' Foscari (Venice, Italy) and the Institut National de la Recherche Scientifique (INRS; Varéennes, Canada) under the supervision of Prof. Patrizia Canton and Prof. Fiorenzo Vetrone. He then undertook a postdoctoral fellowship at the University of Ottawa from 2017 to 2019 with Prof. Eva Hemmer and Prof. Muralee Murugesu. In 2019, he moved with a Marie*

*Skłodowska-Curie individual fellowship at the Universidad Autónoma de Madrid in the group of Prof. Daniel Jaque (nanoBIG), where he is currently a postdoctoral researcher. His research interests span from (nano)materials based on lanthanide ions and semiconductors for biomedical applications to coordination compounds with optomagnetic properties. He is an enthusiast of design and its use to convey scientific results clearly and accessibly to different audiences.*

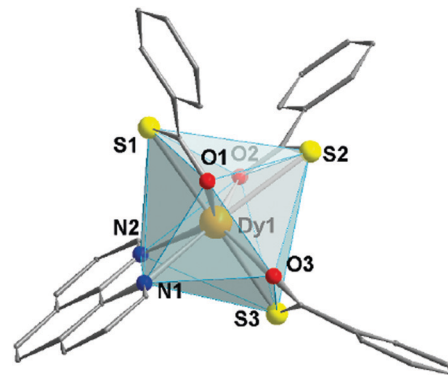


Fig. 1 Partially labelled molecular structure of (**1**). Hydrogen atoms are omitted for clarity. Colour code: Dy – orange; O – red; S – yellow; N – blue.

These DCM molecules evaporate from the lattice when the crystals are exposed to the atmosphere for a prolonged time, resulting in loss of crystallinity. The octa-coordinated  $\text{Dy}^{3+}$  ion adopts a distorted triangular dodecahedron configuration ( $D_{2d}$  maximum symmetry – see Table S2, ESI†) observed in other mononuclear and dinuclear  $\text{Dy}^{3+}$  SMMs.<sup>16,17</sup> The coordination environment of  $\text{Dy}^{3+}$  is composed of three oxygen and three sulphur atoms belonging to the  $\text{tba}^-$  ligands, along with two phen nitrogen atoms. The  $\text{Dy}\cdots\text{O}$  distances range between 2.34 and 2.37 Å, while  $\text{Dy}\cdots\text{S}$  bonds are longer (2.80–2.84 Å). These values are in line with other lanthanide coordination compounds based on  $\text{tba}^-$ .<sup>18,19</sup> Inspection of the packing (Fig. S2, ESI†) reveals a 3D arrangement of the complexes governed by  $\pi$ - $\pi$  stacking (Fig. S3, ESI†) both in the face-to-face and edge-to-face configurations – centroid-to-centroid distances of 3.76 and 4.78 Å, respectively (see ESI† for more details). Within the crystal, the shortest intermolecular  $\text{Dy}\cdots\text{Dy}$  distance is 7.20 Å (Fig. S3, ESI†).

We should point out that in  $\text{Ln}^{3+}$ -complexes Ln–E bonds are less common than Ln–O ones, owing to the weaker interaction between  $\text{Ln}^{3+}$  (hard acid) and E (soft donor). Among E-containing ligands, carbamates, xanthates, and diphenyl chalcogenides are the most studied ones.<sup>20–23</sup> Thiobenzoate has instead been poorly investigated, with only two reported  $\text{Ln}^{3+}$ -tba complexes to date.<sup>18,19</sup> Yet, as observed in **1**, this ligand can promote both magnetic and PL properties in  $\text{Ln}^{3+}$ -complexes, since it provides simultaneously strong and stable Ln–O interaction along with property modulation imparted by Ln–S bonds.

### Magnetic characterization

To investigate the magnetic properties of **1**, the dc (direct current) magnetic susceptibility was first measured between 300–1.8 K under an applied field of 1000 Oe (Fig. S5A, ESI†). The  $\chi T$  product exhibited a gradual decrease from 14.15 to 12.41  $\text{cm}^3 \text{K mol}^{-1}$  upon cooling from 300 to 1.8 K. Its value at room temperature is in good agreement with the theoretical value for a single  $\text{Dy}^{3+}$  ion ( $S = 5/2$ ,  $L = 5$ ,  ${}^6\text{H}_{15/2}$   $g = 4/3$ ,  $C = 14.17 \text{ cm}^3 \text{K mol}^{-1}$ ). The decrease at low temperature can arise

from a combination of thermal depopulation of Stark sublevels, significant magnetic anisotropy, and small yet non-negligible antiferromagnetic intermolecular interactions between  $\text{Dy}^{3+}$  centres.<sup>12</sup> The presence of magnetic anisotropy was confirmed by the field-dependent magnetization observed in the magnetization ( $M$  vs.  $H$ ) and reduced magnetization ( $M$  vs.  $HT^{-1}$ ) plots, which reaches a maximum value of  $5.70 \text{ M}\mu_{\text{B}}$  at  $1.9 \text{ K}$  and  $7 \text{ T}$  (Fig. S5b, ESI†). Therein, the non superimposition of the isofield lines indicates the presence of non negligible magnetic anisotropy (Fig. S5c, ESI†).

The SMM properties of **1** were studied *via ac* (alternating current) susceptibility measurements in the  $0.1$ – $1500 \text{ Hz}$  range with an oscillating field  $H_{\text{ac}} = 3.78 \text{ Oe}$ . Below  $12 \text{ K}$ , frequency-dependent susceptibility was observed (Fig. 2a) indicative of slow relaxation of the magnetization intrinsic to the molecule. In the absence of an external field ( $H_{\text{dc}} = 0 \text{ Oe}$ ), a frequency-dependent signal was observed with a strong contribution of quantum tunnelling of magnetization (QTM) at low temperature. QTM within the ground KD is not fully suppressed despite the good axiality of the  $g$ -tensor of the ground KD ( $g_x = g_y = 0.001$  and  $g_z = 19.832$ ; *vide infra*). This observation is supported by the calculated transition magnetic moment matrix elements between the spin-orbit states in the ground multiplet of  ${}^6\text{H}_{15/2}$  (*vide infra*). To probe the mechanisms responsible for the spin-reversal, the relaxation times ( $\tau$ ) of the individual peaks were extracted from the  $\chi''$  data using the generalized Debye model (Tables S3–S5, ESI†).<sup>24</sup> Considering the most common relaxation mechanisms – Orbach, Raman, and QTM – and the temperature regimes at which they operate, the  $\tau^{-1}$  vs.  $T$  dataset (Fig. 2c and Fig. S6a, ESI†) was fit to the following equation:

$$\tau^{-1} = \tau_0^{-1} \exp[-U_{\text{eff}}/K_{\text{b}}T] + CT^n + B_1/(1 + B_2H^2) \quad (1)$$

The best-fit values (Table S6, ESI†) indicate that **1** acts as a zero-field SMM with thermally activated relaxation *via* the Orbach mechanism ( $U_{\text{eff}} = 136.8 \text{ K} = 95.1 \text{ cm}^{-1}$ ). Spectroscopic analysis supports the attribution of this relaxation through the first excited  $m_j$  level, similarly to what is indicated by calculations (*vide infra*).

To determine the optimal applied dc field that minimizes QTM at low temperature, field-dependent relaxation dynamics were investigated at  $5 \text{ K}$  (Fig. S7, ESI†). Frequency-dependent signals in the out-of-phase  $\chi''$  susceptibility were observed between  $0$  and  $5000 \text{ Oe}$ . The field-dependent  $\tau$  values were obtained fitting the  $\chi''$  susceptibility to the generalized Debye model, and the resulting  $\tau^{-1}$  vs.  $T$  dataset was fit with the following equation (which includes the field-dependent direct, Raman, and QTM mechanisms):

$$\tau^{-1} = AH^4 + CT^n + B_1/(1 + B_2H^2) \quad (2)$$

Introduction of the Orbach (field-independent) term did not lead to a better fit and was hence excluded to avoid over-parametrization. The best-fit values (Table S7, ESI†) indicates that the relaxation dynamics when  $H_{\text{dc}} \leq 450 \text{ Oe}$  are governed by QTM, and for  $H_{\text{dc}} \geq 1800 \text{ Oe}$  the direct mechanism becomes dominant. Hence, an optimal field of  $500 \text{ Oe}$  was chosen to ensure minimal contributions from both mechanisms. Indeed, temperature-dependent ac studies under an external field of  $500 \text{ Oe}$  (Fig. 2b) confirmed the complete suppression of the QTM mechanism (Fig. 2c and Fig. S6b, ESI†). Even after QTM suppression, magnetic relaxation continues to occur *via* the first excited  $m_j$  level ( $138.2 \text{ K} = 96.1 \text{ cm}^{-1}$ ). Magnetic hysteresis measurements revealed no retention of the magnetic moment at  $1.8 \text{ K}$ .

### Optical properties and luminescence thermometry

The combination of ligands and  $\text{Dy}^{3+}$  in **1** yields also augmented the optical properties. The emission spectrum is dominated by the typical  $\text{Ln}^{3+}$  narrow emission lines (Fig. 3a). The excitation spectrum – recorded while monitoring the  $\text{Dy}^{3+}$  emission at  $570 \text{ nm}$  – shows both sharp and broadband features (Fig. 3a), ascribed respectively to the  $4f$ – $4f$   $\text{Ln}^{3+}$  transitions and the organic ligands. The appearance of this latter contribution is indicative of ligand-sensitized emission. In this process, the ligands absorb the excitation photons and transfer the optical energy to the coordinated metal centre, which then relaxes radiatively to its ground state (*i.e.*, emits photons). Upon fitting with a single exponential function the decay curve obtained

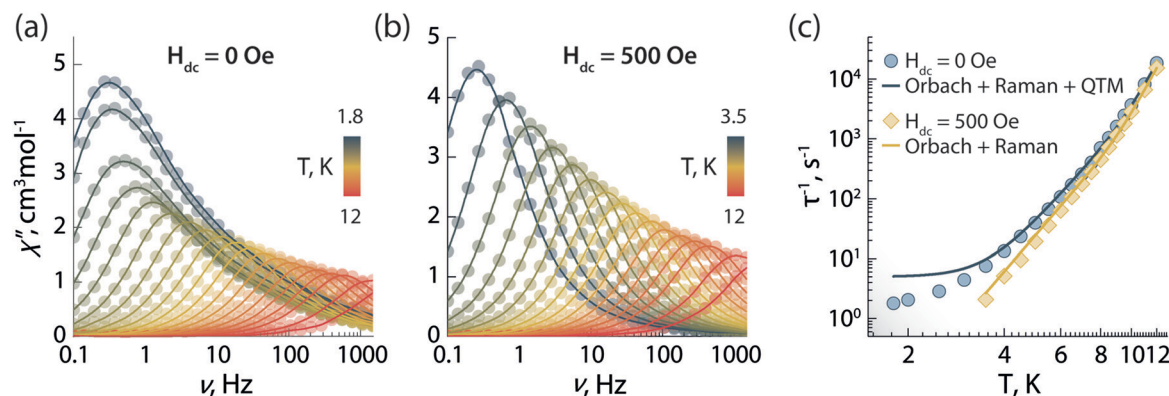
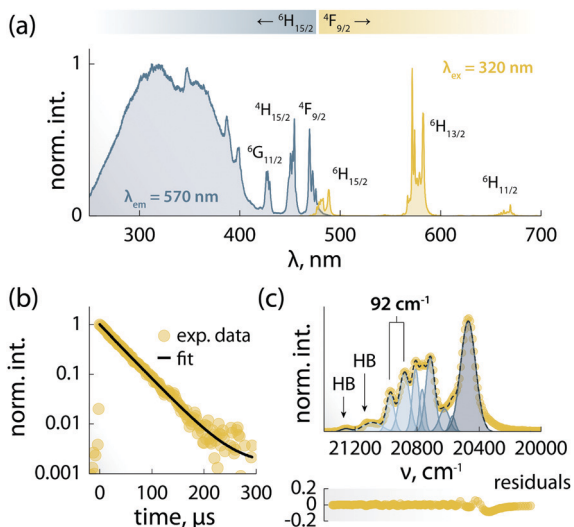


Fig. 2 Frequency dependence of the out-of-phase ( $\chi''$ ) magnetic susceptibility as a function of temperature obtained in absence of an external dc magnetic field (a) and under an applied static field of  $500 \text{ Oe}$  (b). (c) Temperature dependence of the magnetic relaxation times ( $\tau$ ) in absence (blue circles) and in the presence of a  $500 \text{ Oe}$  applied field (yellow diamonds). Solid lines in (c) are the best fit to the experimental data using eqn (1).



**Fig. 3** Spectroscopic studies of **1**. (a) Excitation (blue) and emission (yellow) spectra recorded respectively with  $\lambda_{\text{em}} = 570$  nm and  $\lambda_{\text{ex}} = 320$  nm at 10 K. The main  $\text{Dy}^{3+}$  transitions are labelled. (b) Decay curve recorded at 10 K monitoring the emission at 570 nm ( ${}^4\text{F}_{9/2} \rightarrow {}^6\text{H}_{13/2}$ ) under 320 nm excitation (yellow circles) and its fit to a single-exponential decay (black line). (c) Top: Zoom-in of the  ${}^4\text{F}_{9/2} \rightarrow {}^6\text{H}_{15/2}$  transition (yellow circles) and its fit (dark blue dashed line) obtained from the sum of Gaussian peaks (blue solid lines). Bottom: Residuals ( $R^2 \approx 0.99$ ). The retrieved position of the first two  ${}^6\text{H}_{15/2}$   $m_j$  levels is indicated with vertical lines, along with their energy separation. HB = hot band.

monitoring the  $\text{Dy}^{3+}:{}^4\text{F}_{9/2} \rightarrow {}^6\text{H}_{13/2}$  transition (Fig. 3b), a characteristic decay time of 40  $\mu\text{s}$  was found for the  $\text{Dy}^{3+}$  emitting state ( ${}^4\text{F}_{9/2}$ ). This value is almost 3 times larger than the lifetime of the luminescent  $\text{Dy}^{3+}$ -SMM with thermometric capabilities we recently reported,<sup>6</sup> and similar to the value observed in a dimetallic ZnDy SMM.<sup>4</sup>

The  ${}^4\text{F}_{9/2} \rightarrow {}^6\text{H}_{15/2}$  transition was deconvoluted (Fig. 3c) to garner information regarding the  $m_j$  levels of the ground state ( ${}^6\text{H}_{15/2}$ ), obtaining an energy separation of 92  $\text{cm}^{-1}$  between the first two  $m_j$  levels. This value is in agreement with the calculated energy separation of 107  $\text{cm}^{-1}$  (*vide infra*), and larger than or on par with the values reported for other optomagnetic  $\text{Dy}^{3+}$  complexes.<sup>4,6,25</sup> Moreover, it is close to the energy barriers observed in ac magnetic studies (95.1 and 96.1  $\text{cm}^{-1}$ , without and with applied field, respectively), and hence indicates that the Orbach magnetic relaxation process occurs through the first excited  $m_j$  level.

The PL of the systems shows also sensitivity towards temperature changes, and can thus be employed for thermal monitoring purposes.<sup>12</sup> To study the thermometric performance of **1**, we recorded PL spectra between 10 and 50 K (Fig. 4a). This range encompasses the high end of the temperature window wherein **1** acts as SMM – *i.e.*, < 12 K. As expected, variations in the relative intensities of the Stark components of the  ${}^4\text{F}_{9/2} \rightarrow {}^6\text{H}_{13/2}$  manifold were observed.

The ratio between the intensity integrated over conveniently selected ranges ( $I_1$  and  $I_2$ , as indicated in the inset of Fig. 4a) was chosen as thermometric parameter ( $\Delta = I_2/I_1$ , Fig. 4b). The  $\Delta$  vs.  $T$  dataset was fit to a parabolic function (Table S8, ESI<sup>†</sup>) that, along with its first derivative, was used to determine the relative thermal sensitivity according to the following equation:<sup>26,27</sup>

$$S_r = \frac{1}{\Delta} \frac{\partial \Delta}{\partial T} \quad (3)$$

The obtained relative thermal sensitivity varies between 0.6 and 1.1%  $\text{K}^{-1}$  over the 10–50 K range (Fig. 4c): a performance comparable to the one of other thermometers based on spectral variations within the same manifold<sup>7,9,28</sup> and other

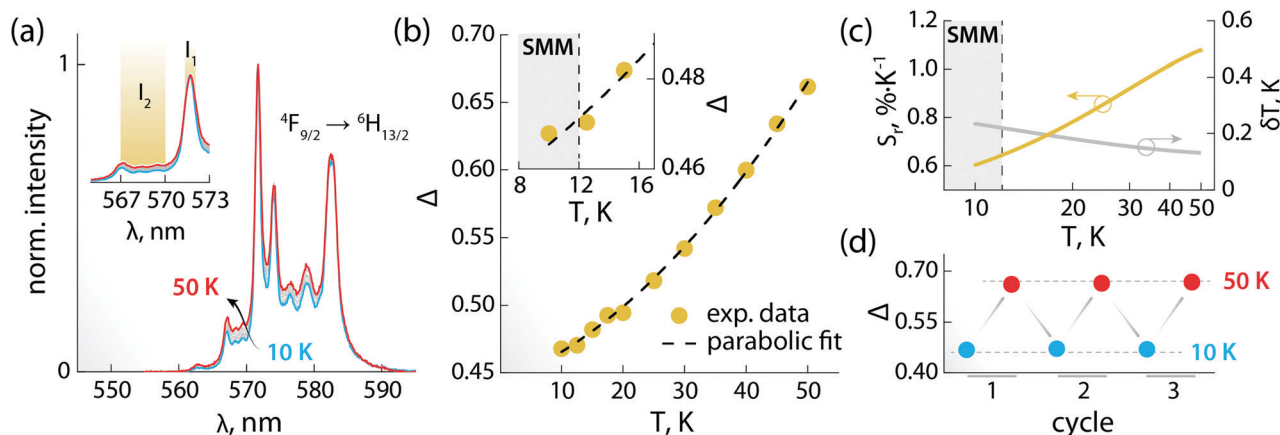


**Fig. 4** Luminescence thermometry performance of **1**. (a) PL spectra recorded in the 10–50 K range under 320 nm excitation. In the inset, a zoom-in of the 565–573 nm range is shown, along with the integration ranges  $I_1$  and  $I_2$  (yellow) used for calculating the areas used to obtain the thermometric parameter ( $\Delta$ ). (b) Calibration curve obtained using the thermometric parameter  $\Delta = I_2/I_1$  (yellow circles) and its fit to a parabolic function (dashed black line). In the inset, a zoom-in of the 8–17 K range is shown. The range wherein **1** behaves as SMM is indicated as a grey rectangle. (c) Relative thermal sensitivity and associated uncertainty calculated from the data in (b) and the mathematical treatment detailed in the ESI<sup>†</sup>. A logarithmic scale is used for the abscissa to better visualize the low-temperature range. (d) Results of three cycles of measurements performed at 10 and 50 K to determine the repeatability of the thermometric approach.

$\text{Ln}^{3+}$ -coordination compounds working in this low-temperature range.<sup>29,30</sup> The uncertainty associated with the thermal reading varies between 0.1 and 0.2 K, while the repeatability of the thermometric approach is 98.9% (Fig. 4d and Table S9, ESI†). The obtained uncertainty is in line with typical values found for measurements performed with photomultipliers.<sup>27</sup> Details about the mathematical treatment of the data are given in the ESI.† Notably, within the temperature range where the complex behaves as SMM, the thermometric approach holds (grey rectangles in Fig. 4b and c). This observation opens the door to the thermal monitoring of **1** via PL during its operation as an SMM: if overheating is optically detected, corrective actions could be taken to avoid failure (e.g., operation interruption or further cooling). Note that, although the relative thermal sensitivity of this complex is lower than the one of the other reported zero-field SMM (based on  $\text{Ho}^{3+}$ ),<sup>31</sup> the data treatment required here is much less laborious. Indeed, a careful background subtraction necessary to isolate 4f–4f reabsorption features from the ligand emission is not required. This aspect makes the proposed system/approach more straightforwardly implementable in real-life applications.

### Theoretical modelling of the chalcogen atom effects

Stimulated by the experimental results, we decided to model the effect of hard (O) and soft (S, Se, and Te) donor atoms on the magnetic and optical properties of the reported optomagnetic complex (Tables S10–S24, ESI†). Specifically, we were interested in the general trends that could serve as a predictive tool to fine-tune simultaneously the magnetic, optical, and thermometric performance of a  $\text{Ln}^{3+}$ -SMM. With this goal in mind, density functional theory (DFT) and CASSCF/RASSI calculations were performed on systems **1<sub>O</sub>**, **1<sub>S</sub>**, **1<sub>Se</sub>**, and **1<sub>Te</sub>**, containing benzoate ( $\text{ba}^-$ ), thiobenzoate ( $\text{tba}^-$ ), selenobenzoate ( $\text{sba}^-$ ), and tellurobenzoate ( $\text{teba}^-$ ), respectively (Fig. 5). The results show that in **1<sub>O</sub>**, the stabilization and axially of the ground Kramers doublet (KD; Table S13, ESI†) are lost. Hence,

a low  $U_{\text{eff}}$  ( $32 \text{ cm}^{-1}$ ) and significant QTM within the ground KD are observed. However, the microscopic magnetic properties and energy spectrum of the  $^6\text{H}_{15/2}$  ground multiplet drastically change in **1<sub>S</sub>**, **1<sub>Se</sub>**, and **1<sub>Te</sub>** compared to **1<sub>O</sub>**. The height of the energy spectrum is increased (Fig. S8, ESI†), the ground KD is more stabilized, the axially of the lowest KDs is improved (as evinced from the calculated g-tensors (Fig. 6a) and crystal field parameters), the main magnetic axes of the lowest KDs are more collinear (Fig. S9, ESI†), and the calculated qualitative energy barriers are higher (Fig. 6b and Tables S13–S16, ESI†). Overall, among **1<sub>S</sub>**, **1<sub>Se</sub>**, and **1<sub>Te</sub>**, the latter has the best parameters by a slight margin: a result of the elongation and decrease in the ionic nature of Ln–E bonds when descending the chalcogen group.§ This is shown by the optimized geometries and calculated electron densities ( $\rho(r)$ ), Laplacians ( $\nabla^2\rho(r)$ ), delocalization indices (DI), and effective atomic charges obtained from the quantum theory of atoms in molecules analysis (Table S23, ESI†). Since the longer radical extensions of the valence orbitals of heavier chalcogens weaken the equatorial crystal ligand field around  $\text{Dy}^{3+}$ , O and N atoms of the carbonyl groups and phen ligand, respectively, start to dominate the axial crystal ligand field of  $\text{Dy}^{3+}$  ion in **1<sub>S</sub>**, **1<sub>Se</sub>**, and **1<sub>Te</sub>**. The weakening of the equatorial ligand field around the  $\text{Dy}^{3+}$  ion has been proven to improve the axially and SMM properties of  $\text{Dy}^{3+}$ -based SMMs in tandem.<sup>5,32</sup> This is best illustrated by investigating the calculated crystal-field parameters ( $B_k^q$ ) and visualizing the main magnetic axis of  $\text{Dy}^{3+}$  ion in the studied systems. For all other systems, except for **1<sub>O</sub>**, the axial crystal-field parameter  $B_0^2$  dominates the crystal ligand field because its value is order of magnitude larger than the values of any other crystal-field parameters, whereas for **1<sub>O</sub>** the non-axial crystal-field parameters are of the same magnitude or even larger than the axial crystal-field parameters for all values of  $k$  (Tables S17–S21, ESI†). Moreover, the visualization of the main magnetic axis of the first three KDs of  $\text{Dy}^{3+}$  ion reveals that they are almost collinear in all other system expect in **1<sub>O</sub>** because of the stronger axially observed in the heavier chalcogen systems (Fig. S9, ESI†). These findings are in line with previous studies on  $\text{Ln}^{3+}$ -based SMMs containing soft donor atoms from the chalcogen groups.<sup>14,33</sup>

The nature of chalcogen atom influences the optical properties of the complex and its expected luminescence thermometry performance too. In this study, we have harnessed the spectral changes arising from temperature-induced population



Fig. 5 Benzoate, thiobenzoate, selenobenzoate, and tellurobenzoate ligands, along with the corresponding complexes derived from **1**.

§ Due to the core-like nature of the 4f orbitals, it is expected that the lanthanides interact with the coordinating ligands through an electrostatic interaction rather than form a covalent bond. However, recent publications have shown that there can be a non-negligible covalent contribution to the bonding in the lanthanide complexes (Aravena *et al.*, *Inorg. Chem.*, 2016, 55, 4457–4469; Briganti *et al.*, *Chem. Sci.*, 2019, 10, 7233–7245; Panetti *et al.*, *Nat. Commun.*, 2021, 12, 1731). For the investigated systems, the AIM analyses support that the electrostatic interactions dominates the interaction between the coordinating ligands and  $\text{Dy}^{3+}$  ion, but this does not automatically rule out the plausible covalent contribution. Indeed, the values of  $\nabla^2\rho(r)$  and DI for Ln–E bonds simultaneously decrease and increase, respectively, when descending the group 16. The results indicate that the covalent contribution of Ln–E bond gradually increases, when going from O to Te, albeit its ionic nature.



Fig. 6 The effects of changing the chalcogen atom in the benzoate ligand on the magnetic and optical properties. Components of the  $g$ -tensor ( $g_x$ ,  $g_y$ ,  $g_z$ ) of the first three KDs (a) and energy of KD2 (b) for the  $\text{Dy}^{3+} \cdot {}^6\text{H}_{15/2}$  ground multiplet of  $\mathbf{1}_o$ ,  $\mathbf{1}_s$ ,  $\mathbf{1}_{Se}$ , and  $\mathbf{1}_{Te}$ . Scheme depicting the temperature-induced electron population redistribution between the KDs (*i.e.*,  $m_j$  levels) of the  $\text{Dy}^{3+} \cdot {}^4\text{F}_{9/2}$  excited state (c). Ratio between the electron population of KD2 and KD1 as obtained from the Boltzmann model for  $\mathbf{1}_o$ ,  $\mathbf{1}_s$ ,  $\mathbf{1}_{Se}$ , and  $\mathbf{1}_{Te}$  (d). The results of the same calculations for  $\mathbf{1}$  (solid gray line, beneath  $\mathbf{1}_o$ ) and considering the position of the  ${}^4\text{F}_{9/2}$  components obtained from the deconvolution (Fig. S11, ESI<sup>†</sup>) of the  ${}^6\text{H}_{15/2} \rightarrow {}^4\text{F}_{9/2}$  transition in the excitation spectrum (exp, dashed yellow line) are also reported. The overlap between the curves  $\mathbf{1}$  and  $\mathbf{1}_o$  is a serendipitous result stemming from the similar energy difference between the first two  ${}^4\text{F}_{9/2}$   $m_j$  levels obtained for these two systems. Energy of the first singlet ( $S_1$ ) and triplet ( $T_1$ ) excited states of the different ligands calculated by the CAM-B3LYP exchange-correlation functional (e). The position of the  $\text{Dy}^{3+} \cdot {}^4\text{F}_{9/2}$  excited state is also indicated with a dashed black line (centroid of the  ${}^4\text{F}_{9/2}$  manifold obtained from the deconvolution of the  ${}^6\text{H}_{15/2} \rightarrow {}^4\text{F}_{9/2}$  transition in the excitation spectrum – Fig. S10, ESI<sup>†</sup>).

redistribution between the  $m_j$  levels (*i.e.*, KDs) to define a ratiometric thermometric approach (Fig. 4). Specifically, the integrated intensity  $I_2$  mainly contains contributions from hot bands (HBs), *i.e.*, transitions from the  $\text{Dy}^{3+} \cdot {}^4\text{F}_{9/2}$  excited  $m_j$  levels to the  $\text{Dy}^{3+} \cdot {}^6\text{H}_{13/2}$  state (Fig. 6c).  $I_1$  has its major contribution stemming from the lowest  $\text{Dy}^{3+} \cdot {}^4\text{F}_{9/2}$   $m_j$  level. The population of each level ( $N_i$ ) as a function of temperature can be modelled with a system of equations based on the Boltzmann function (see ESI<sup>†</sup> for details). Since the intensity ratio is proportional to the electron population, and considering the low temperature range investigated, the ratio between the electron population of the first excited level and ground level ( $N_2/N_1$ ) can thus approximate the intensity ratio  $\Delta = I_2/I_1$  used for the thermometric approach. This assumption is corroborated by the overlap between the  $N_2/N_1$ -vs.-temperature curves (Fig. 6d) for  $\mathbf{1}$  and using the energy values extracted from the deconvolution of the  ${}^6\text{H}_{15/2} \rightarrow {}^4\text{F}_{9/2}$  transition in the excitation spectrum (Fig. S11, ESI<sup>†</sup>). Because of the effect that different chalcogen atoms have on the  $\text{Dy}^{3+} \cdot {}^4\text{F}_{9/2}$   $m_j$  levels separation (Tables S13–S16, ESI<sup>†</sup>), the  $N_2/N_1$  curve becomes steeper and has an earlier onset following the order  $\mathbf{1}_{Te} > \mathbf{1}_{Se} > \mathbf{1}_s > \mathbf{1}_o$  (Fig. 6d). These observations indicate that a thermometric approach based on the fine structure of the  ${}^4\text{F}_{9/2} \rightarrow {}^6\text{H}_{13/2}$  manifold is more sensitive and can extend to lower temperatures using heavier chalcogens.

Thus, it appears that moving downwards along the chalcogen group can be a viable strategy to simultaneously boost the magnetic properties and luminescence thermometry performance of luminescent  $\text{Ln}^{3+}$ -SMMs. However, there is an additional piece of the puzzle to consider: the lower energy of the first excited singlet ( $S_1$ ) and triplet ( $T_1$ ) states of heavy-chalcogen-containing ligands. Indeed, the calculated energies of these states decrease in the following order:  $\mathbf{1}_o > \mathbf{1}_s > \mathbf{1}_{Se} > \mathbf{1}_{Te}$ . It is therefore possible that the  $S_1$  or  $T_1$  or both states of the chalcogen ligand fall too close or even below the emitting  $\text{Dy}^{3+} \cdot {}^4\text{F}_{9/2}$  state. In that case, lack of sensitization or efficient quenching of the lanthanide PL due to back energy transfer to the ligand would occur.

It should be pointed out that the observations based on the modelled  $\text{Dy}^{3+}$  ground state ( ${}^6\text{H}_{15/2}$ ) are reliable, as confirmed by the good match between the  $m_j$  levels retrieved from the *ab initio* calculations and the deconvolution of the  ${}^4\text{F}_{9/2} \rightarrow {}^6\text{H}_{15/2}$  transition (Fig. S10, ESI<sup>†</sup>). However, modelling of the excited states is generally less accurate, and the absolute energy values of spin-orbit states are accompanied by a large error (Fig. S11, ESI<sup>†</sup>). This discrepancy also applies to the simulated thermometric performance of the complexes (Fig. 6d). For this reason, particularly for the optical properties of the complexes, we analysed relative trends instead of absolute values. From these trends, a positive effect seems to be played by the introduction

of soft chalcogen donors in the Dy<sup>3+</sup> coordination sphere both in terms of magnetism and *m<sub>j</sub>*-level-based luminescence thermometry. Yet, the lowering of the ligand states' energy could frustrate these beneficial effects, up to a complete quenching of Dy<sup>3+</sup> emission.

## Conclusions

In conclusion, we reported the first thiobenzoate-based Ln<sup>3+</sup>-SMM in the form of a mononuclear Dy<sup>3+</sup> complex. Slow relaxation of the magnetization under no applied field was observed up to 12 K. The mechanisms involved in this process were interpreted combining analysis of magnetic data, photoluminescence spectrum, and theoretical calculations. A ratiometric luminescence thermometry approach was established harnessing the thermal dependence of Dy<sup>3+</sup> emission, with a relative thermal sensitivity between 0.6 and 1.1%·K<sup>-1</sup> and temperature uncertainty well below 1 K across the 10–50 K temperature range. We subsequently used this complex as a model system to investigate how the introduction of different chalcogen donors (O, S, Se, Te) in the metal coordination sphere impact on the magnetic, optical, and luminescence thermometry performance. The trends obtained from *ab initio* calculations indicate that softer chalcogen donors can simultaneously boost the SMM performance and the sensitivity of thermometric approaches based on variations of the Stark levels' intensity. On the other hand, lowering of the energy states of the chalcogen-bearing ligand could result in an unfavourable energy scheme, and hence ultimately loss of appreciable Dy<sup>3+</sup> emission.

Overall, this novel optomagnetic complex is a remarkable example of how the use of ligands that combine the features of soft (S, Se, and Te) and hard (O) donors (*i.e.*, electronic cloud modulation and strong/weak interaction with the metal centre) is a promising strategy for the preparation of Ln<sup>3+</sup>-SMMs with tailored optical properties. Moreover, the general considerations obtained from modelling of the family of complexes used herein as case study are envisaged to support the design of novel multifunctional Ln<sup>3+</sup>-complexes based on soft-donor-bearing ligands that combine magnetic, optical, and luminescence thermometry properties.

## Author contributions

R. M. – conceptualization, data curation, formal analysis, funding acquisition, investigation, methodology, visualization, writing original draft. D. A. G. – formal analysis, investigation, methodology, writing original draft. R. G. – formal analysis, methodology, writing original draft. J. O. M. – formal analysis, funding acquisition, supervision, methodology, writing original draft. L. D. C. – supervision, writing – review & editing. D. J. – supervision, writing – review & editing. M. M. – supervision, writing – review & editing.

## Conflicts of interest

There are no conflicts to declare.

## Acknowledgements

R. M. acknowledges the support of the European Commission through the European Union's Horizon 2020 research and innovation program under the Marie Skłodowska-Curie Grant agreement 797945 (LANTERNS). This work was supported by Ministerio de Ciencia e Innovación de España (PID2019-106211RB-I00) and developed within the scope of the project CICECO-Aveiro Institute of Materials, UIDB/50011/2020, financed by Portuguese funds through FCT/MEC and co-financed by FEDER under the PT2020 Partnership Agreement. We thank the University of Ottawa, the CFI, and the NSERC for financial support of this work. J. O. M. and R. G. acknowledge Academy of Finland (project numbers 315829, 320015, and 345484) for funding. CSC-IT Centre for Science in Finland, the Finnish Grid and Cloud Infrastructure (persistent identifier urn:nbn:fi:research-infras-2016072533) and Prof. H. M. Tuononen (University of Jyväskylä) are acknowledged for providing computational resources for the project. We are greatly indebted to Dr Josefina Perles Hernáez from the Interdepartmental Investigation Service (SID) of the Universidad Autónoma de Madrid for performing the X-ray diffraction experiment and solving the crystal structure of the complex investigated.

## References

- 1 F. Arute, K. Arya, R. Babbush, D. Bacon, J. C. Bardin, R. Barends, R. Biswas, S. Boixo, F. Brandao, D. A. Buell, B. Burkett, Y. Chen, Z. Chen, B. Chiaro, R. Collins, W. Courtney, A. Dunsworth, E. Farhi, B. Foxen, A. Fowler, C. Gidney, M. Giustina, R. Graff, K. Guerin, S. Habegger, M. P. Harrigan, M. J. Hartmann, A. Ho, M. Hoffmann, T. Huang, T. S. Humble, S. V. Isakov, E. Jeffrey, Z. Jiang, D. Kafri, K. Kechedzhi, J. Kelly, P. V. Klimov, S. Knysh, A. Korotkov, F. Kostritsa, D. Landhuis, M. Lindmark, E. Lucero, D. Lyakh, S. Mandra, J. R. McClean, M. McEwen, A. Megrant, X. Mi, K. Michielsen, M. Mohseni, J. Mutus, O. Naaman, M. Neeley, C. Neill, M. Y. Niu, E. Ostby, A. Petukhov, J. C. Platt, C. Quintana, E. G. Rieffel, P. Roushan, N. C. Rubin, D. Sank, K. J. Satzinger, V. Smelyanskiy, K. J. Sung, M. D. Trevithick, A. Vainsencher, B. Villalonga, T. White, Z. J. Yao, P. Yeh, A. Zalcman, H. Neven and J. M. Martinis, *Nature*, 2019, **574**, 505–510.
- 2 D. N. Woodruff, R. E. Winpenney and R. A. Layfield, *Chem. Rev.*, 2013, **113**, 5110–5148.
- 3 J. Long, Y. Guari, R. A. S. Ferreira, L. D. Carlos and J. Larionova, *Coord. Chem. Rev.*, 2018, **363**, 57–70.
- 4 J. Long, J. Rouquette, J. M. Thibaud, R. A. Ferreira, L. D. Carlos, B. Donnadieu, V. Vieru, L. F. Chibotaru, L. Konczewicz, J. Haines, Y. Guari and J. Larionova, *Angew. Chem., Int. Ed.*, 2015, **54**, 2236–2240.
- 5 F. S. Guo, B. M. Day, Y. C. Chen, M. L. Tong, A. Mansikkamaki and R. A. Layfield, *Science*, 2018, **362**, 1400–1403.

- 6 D. Errulat, R. Marin, D. A. Galico, K. L. M. Harriman, A. Pialat, B. Gabidullin, F. Iikawa, O. D. D. Couto Jr., J. O. Moilanen, E. Hemmer, F. A. Sigoli and M. Murugesu, *ACS Cent. Sci.*, 2019, **5**, 1187–1198.
- 7 G. Brunet, R. Marin, M. J. Monk, U. Resch-Genger, D. A. Galico, F. A. Sigoli, E. A. Suturina, E. Hemmer and M. Murugesu, *Chem. Sci.*, 2019, **10**, 6799–6808.
- 8 D. A. Galico, R. Marin, G. Brunet, D. Errulat, E. Hemmer, F. A. Sigoli, J. O. Moilanen and M. Murugesu, *Chem. – Eur. J.*, 2019, **25**, 14625–14637.
- 9 M. Fondo, J. Corredoira-Vázquez, A. M. García-Deibe, J. Sanmartín-Matalobos, M. Amozá, A. M. P. Botas, R. A. S. Ferreira, L. D. Carlos and E. Colacio, *Inorg. Chem. Front.*, 2020, **7**, 3019–3029.
- 10 R. A. S. Ferreira, E. Mamontova, A. M. P. Botas, M. Shestakov, J. Vanacken, V. Moshchalkov, Y. Guari, L. F. Chibotaru, D. Luneau, P. S. André, J. Larionova, J. Long and L. D. Carlos, *Adv. Opt. Mater.*, 2021, **9**, 2101495.
- 11 A. N. Carneiro Neto, E. Mamontova, A. M. P. Botas, C. D. S. Brites, R. A. S. Ferreira, J. Rouquette, Y. Guari, J. Larionova, J. Long and L. D. Carlos, *Adv. Opt. Mater.*, 2021, **10**, 2101870.
- 12 R. Marin, G. Brunet and M. Murugesu, *Angew. Chem., Int. Ed.*, 2021, **60**, 1728–1746.
- 13 F. Tuna, C. A. Smith, M. Bodensteiner, L. Ungur, L. F. Chibotaru, E. J. McInnes, R. E. Winpenny, D. Collison and R. A. Layfield, *Angew. Chem., Int. Ed.*, 2012, **51**, 6976–6980.
- 14 A. B. Canaj, S. Dey, O. Cespedes, C. Wilson, G. Rajaraman and M. Murrie, *Chem. Commun.*, 2020, **56**, 1533–1536.
- 15 G. A. Kumar, R. E. Riman and J. G. Brennan, *Coord. Chem. Rev.*, 2014, **273–274**, 111–124.
- 16 J. Xi, X. Ma, P. Cen, Y. Wu, Y. Q. Zhang, Y. Guo, J. Yang, L. Chen and X. Liu, *Dalton Trans.*, 2021, **50**, 2102–2111.
- 17 W. Huang, Z. Zheng and D. Wu, *Inorg. Chem. Commun.*, 2017, **84**, 40–44.
- 18 L. Tian and J. J. Vittal, *Cryst. Growth Des.*, 2006, **6**, 822–824.
- 19 T. Kanda, M. Ibi, K.-I. Mochizuki and S. Kato, *Chem. Lett.*, 1998, 957–958.
- 20 M. D. Regulacio, M. H. Pablico, J. A. Vasquez, P. N. Myers, S. Gentry, M. Prushan, S. W. Tam-Chang and S. L. Stoll, *Inorg. Chem.*, 2008, **47**, 1512–1523.
- 21 S.-S. Liu, J.-M. Zhao, S. Deng, J. Xiong, M.-F. Yang, J.-X. Li, S.-J. Lin, Y.-Q. Zhang and B.-W. Wang, *Inorg. Chem. Commun.*, 2018, **95**, 82–85.
- 22 D. Brown and D. G. Holah, *Chem. Commun.*, 1968, 1545–1546.
- 23 J. H. Melman and T. J. Emge, *Chem. Commun.*, 1997, 2269–2270.
- 24 S. M. J. Aubin, Z. Sun, L. Pardi, J. Krzystek, K. Folting, L.-C. Brunel, A. L. Rheingold, G. Christou and D. N. Hendrickson, *Inorg. Chem.*, 1999, **38**, 5329–5340.
- 25 Y. Xin, J. Wang, M. Zychowicz, J. J. Zakrzewski, K. Nakabayashi, B. Sieklucka, S. Chorazy and S. I. Ohkoshi, *J. Am. Chem. Soc.*, 2019, **141**, 18211–18220.
- 26 S. A. Wade, S. F. Collins and G. W. Baxter, *J. Appl. Phys.*, 2003, **94**, 4743–4756.
- 27 C. D. S. Brites, A. Millán and L. D. Carlos, in *Handbook on the Physics and Chemistry of Rare Earths*, ed., J.-C. G. Bünzli, V. K. Pecharsky, Elsevier Science, B. V. Amsterdam, 2016, vol. 49, pp. 339–427.
- 28 A. Skripka, A. Morinvil, M. Matulionyte, T. Cheng and F. Vetrone, *Nanoscale*, 2019, **11**, 11322–11330.
- 29 L. Li, Y. Zhu, X. Zhou, C. D. S. Brites, D. Ananias, Z. Lin, F. A. A. Paz, J. Rocha, W. Huang and L. D. Carlos, *Adv. Funct. Mater.*, 2016, **26**, 8677–8684.
- 30 G. Bao, K. L. Wong, D. Jin and P. A. Tanner, *Light: Sci. Appl.*, 2018, **7**, 96.
- 31 J. Wang, J. J. Zakrzewski, M. Zychowicz, V. Vieru, L. F. Chibotaru, K. Nakabayashi, S. Chorazy and S. I. Ohkoshi, *Chem. Sci.*, 2020, **12**, 730–741.
- 32 H. S. Wang, K. Zhang, J. Wang, Z. B. Hu, Z. Zhang, Y. Song and Y. Q. Zhang, *Inorg. Chem.*, 2021, **60**, 9941–9955.
- 33 K. R. Vignesh, D. I. Alexandropoulos, B. S. Dolinar and K. R. Dunbar, *Dalton Trans.*, 2019, **48**, 2872–2876.